

Extending *Gaia* DR2 with *HST* narrow-field astrometry. II. Refining the method on WISE J163940.83–684738.6*

L. R. Bedin^{1†} and C. Fontanive²

¹*INAF-Osservatorio Astronomico di Padova, Vicolo dell'Osservatorio 5, I-35122 Padova, Italy*

²*Center for Space and Habitability, University of Bern, Gesellschaftsstrasse 6, 3012 Bern, Switzerland*

Accepted 2020 February 21. Received 2020 February 21; in original form 2020 January 28

ABSTRACT

In the second paper of this series we perfected our method of linking high precision *Hubble Space Telescope* astrometry to the high-accuracy *Gaia* DR2 absolute reference system to overcome the limitations of relative astrometry with narrow-field cameras. Our test case here is the Y brown dwarf WISE J163940.83–684738.6, observed at different epochs spread over a 6-yr time baseline with the *Infra-Red* channel of the *Wide Field Camera 3*. We derived significantly improved astrometric parameters compared to previous determinations, finding: $(\mu_{\alpha \cos \delta}, \mu_{\delta}, \varpi) = (577.21 \pm 0.24 \text{ mas yr}^{-1}, -3108.39 \pm 0.27 \text{ mas yr}^{-1}, 210.4 \pm 1.8 \text{ mas})$. In particular, our derived absolute parallax (ϖ) corresponds to a distance of $4.75 \pm 0.05 \text{ pc}$ for the faint ultracool dwarf.

Key words: brown dwarfs: individual (WISE J163940.83–684738.6)

1 INTRODUCTION

Distance is a crucial parameter for investigating the basic physical properties of any astronomical object. Indeed, precise distances are essential to connect measured properties to intrinsic characteristics (e.g. apparent to absolute magnitude), and therefore to compare observations to theoretical predictions.

Current atmospheric and evolutionary models struggle to reproduce the photometric properties of the lowest-mass and coolest brown dwarfs (Schneider et al. 2016; Leggett et al. 2017). Measurements of accurate distances allow for the determination of absolute fluxes and unbiased spectral energy distributions, making such measurements a necessary step to improve characterisation and modelling of low-mass objects (e.g. Kirkpatrick et al. 2019). Precise distance estimates can also be used to compare the appearance of individual objects to well-calibrated colour-magnitude diagrams. In particular, the identification of outliers along the standardised locus can probe secondary attributes of these substellar objects. For example, over-luminous sources may be indicative of unresolved binarity (Manjavacas et al. 2013; Tinney et al. 2014; Kirkpatrick et al. 2019). Likewise, excessively red or blue colours can trace a deviant surface gravity or metallicity, or be evidence for diverse atmospheric

features like clouds (Knapp et al. 2004; Chiu et al. 2006; Cruz et al. 2007, 2009).

Finally, the study of well-defined and complete samples in space allows for the development and testing of formation and evolution theories (e.g. Kirkpatrick et al. 2019). Current observations of substellar mass functions and space densities are in tension with model predictions (Burgasser 2004; Allen et al. 2005; Pinfield et al. 2006; Kirkpatrick et al. 2012). High-confidence volume-limited samples can only be achieved through measurements of distances, which are thus required to obtain a comprehensive portrait of the local substellar population.

Parallaxes are the most direct measures of distance for stellar and substellar objects. With the extensive sky coverage of large astrometric missions (e.g. *Gaia*, *Hipparcos*), most stars in the solar neighbourhood and nearby moving groups or star-forming regions have reliable parallax measurements. Isolated brown dwarfs and free-floating planetary-mass objects, on the other hand, are generally too faint and too red to be detected by these broad surveys, and very few substellar objects are typically included in these astrometric catalogues.

Spectrophotometric distances (based on expected relations between absolute magnitude and spectral type or apparent photometry) are often the only viable way to estimate distances for intrinsically faint objects. However, significant disagreements have been found between model-derived spectrophotometric distances and parallactic measurements (e.g. Kirkpatrick et al. 2011, 2012), and the former estimates are often viewed as unreliable (Cushing et al. 2011; Liu et al. 2011). Some dedicated programs aim at deriving trigonomet-

* Based on observations with the NASA/ESA *Hubble Space Telescope*, obtained at the Space Telescope Science Institute, which is operated by AURA, Inc., under NASA contract NAS 5-26555.
† E-mail: luigi.bedin@oapd.inaf.it

ric parallaxes for brown dwarfs, such as the Hawaii Infrared Parallax Program (Dupuy & Liu 2012; Liu et al. 2016) or the Brown Dwarf Kinematics Project (Faherty et al. 2012) (see also Dupuy & Kraus 2013; Manjavacas et al. 2013, 2019; Martin et al. 2018; Kirkpatrick et al. 2019 for other compilations of parallactic distances). Despite these remarkable efforts, the typical precision reached in these observationally-expensive campaigns results in substantial uncertainties in the underlying distances, and large inconsistencies remain between programs for the faintest targets (e.g. Beichman et al. 2014).

We recently devised in Bedin & Fontanive (2018) (hereafter, Paper I) a new method to improve the astrometric precision of *Hubble Space Telescope* (*HST*) observations and derive astrometric parameters with *Gaia*-level precisions for sources too faint to be detected with *Gaia*. This provides a powerful procedure to infer highly-precise distances for faint, ultracool brown dwarfs. For our test case target, the Y1 brown dwarf WISE J154151.65–225024.9 (Cushing et al. 2011; Schneider et al. 2015), we achieved a precision at the milli-arcsecond (mas) level on parallax and at the sub-mas level on proper motion, improving by an order of magnitude the uncertainties from previous estimates.

In this paper, we further improve our method and apply it to the Y dwarf WISE J163940.83–684738.6 in order to constrain its astrometric parameters to unprecedented levels.

2 W1639–6847

WISE J163940.83–684738.6 (hereafter W1639–6847) was first reported by Tinney et al. (2012), after using ground-based methane imaging to carefully resolve the near-infrared counterpart of a blended WISE source. The authors estimated a Y0–Y0.5 spectral type based on near-infrared spectroscopy. Tinney et al. (2014) subsequently found W1639–6847 to show under-luminous *J* and *W2* absolute magnitudes and to be more consistent with a later type of Y0.5. The authors also concluded that some photometric properties of the brown dwarf were in better agreement with Y1 brown dwarfs. Using *HST* spectroscopy, Schneider et al. (2015) found that the *J*-band peak of W1639–6847 matched well with the Y0 spectral standard, in agreement with previous spectral type estimates. However, the *Y*-band peak appeared to be significantly blue-shifted when compared to the T9 spectral standard, and *Y* – *J* colour seemed unusual relative to other Y0 dwarfs. This led Schneider et al. (2015) to classify W1639–6847 as Y0-Peculiar (Y0pec), which is since the adopted spectral type of this object.

Opitz et al. (2016) studied W1639–6847 as part of a multiplicity survey, attempting to resolve close Y dwarf binaries with the Gemini Multi-Conjugate Adaptive Optics System. The authors were able to rule out secondary companions down to 3.5 mag fainter from separations beyond 0.5 AU. However, the search for companions was limited to the inner 2.5 AU around the primary. No search for wide binary companion around W1639–6847 is reported in the literature to this date.

From atmospheric fits to the observed spectrum and photometry of W1639–6847, Schneider et al. (2015) esti-

mated an effective temperature of 400 K and a high surface gravity for the target, although such model-derived physical characteristics are likely to be somewhat unreliable (Schneider et al. 2015). Based on Gemini spectroscopic data, Leggett et al. (2017) derived a similar effective temperature (360–390 K) as Schneider et al. (2015), but found a lower surface gravity. Using evolutionary models, they obtained a mass of 5–14 M_{Jup} for an age of 0.5–5 Gyr. More recently, Zalesky et al. (2019) performed detailed atmospheric retrieval analyses on late-T and Y brown dwarfs using *HST* data. While the large majority of their studied objects appeared consistent with the physics of radiative-convective equilibrium, the retrieved structure for W1639–6847 was strongly deviating from typical temperature-pressure profiles under the assumption of radiative-convective equilibrium. The obtained fit provided rather unrealistic results, with a high effective temperature of ~ 650 K, and very small radius ($0.5 R_{\text{Jup}}$) and mass values ($1.5 M_{\text{Jup}}$). The authors concluded that their data-driven atmospheric retrieval was poorly adapted to explain the deviant physical characteristics of this unique ultracool brown dwarf.

As noted by several authors, the majority of such analyses are highly sensitive to the adopted distances of the studied objects. Tinney et al. (2012) initially derived a parallactic distance of 5.0 ± 0.5 pc for W1639–6847. They also reported a very large proper motion (~ 3 arcsec yr $^{-1}$) and measured a significant tangential velocity. They deduced from kinematics arguments that the source was likely older than the overall field population, in agreement with Leggett et al. (2017) who found it to be consistent with thin disk membership. Tinney et al. (2014) then refined the proper motion and parallax estimates, significantly reducing the size of previous uncertainties. Recent work by Martin et al. (2018) and Kirkpatrick et al. (2019) provided updated astrometry for W1639–6847 based on *Spitzer* images, refining its distance to $4.39^{+0.18}_{-0.17}$ pc (Martin et al. 2018) and 4.72 ± 0.06 pc (Kirkpatrick et al. 2019), respectively. Existing results on parallax based on various datasets remain discrepant by up to 2.9σ . Additional and independent reliable astrometric measurements of W1639–6847 will thus be crucial to understand the nature and further characterise the peculiar features of this distinct object.

3 OBSERVATIONS

W1639–6847 was observed at three different epochs with the Wide Field Camera 3 (WFC3) instrument onboard the *Hubble Space Telescope* (*HST*). All data were collected using the infrared (IR) channel of WFC3. The first epoch was acquired as part of program GO 12970 (PI: Cushing), on February 15th 2013. The second epoch consists of three sub-epochs obtained as part of the same program on October 26th, 27th and 29th 2013. A final orbit of observations was taken on March 11th 2019 for GO 15201 (PI: Fontanive).

The first visit was obtained in the WFC3/IR F125W filter. It was split into 4 dithered images of 602.937 s exposure each, for a total exposure time of 2411.749 s. Each image was taken in MultiAccum mode with NSAMP=14 samplings and using the sequence SAMP-SEQ=SPARS50.

The photometric data acquired for W1639–6847 on Oc-

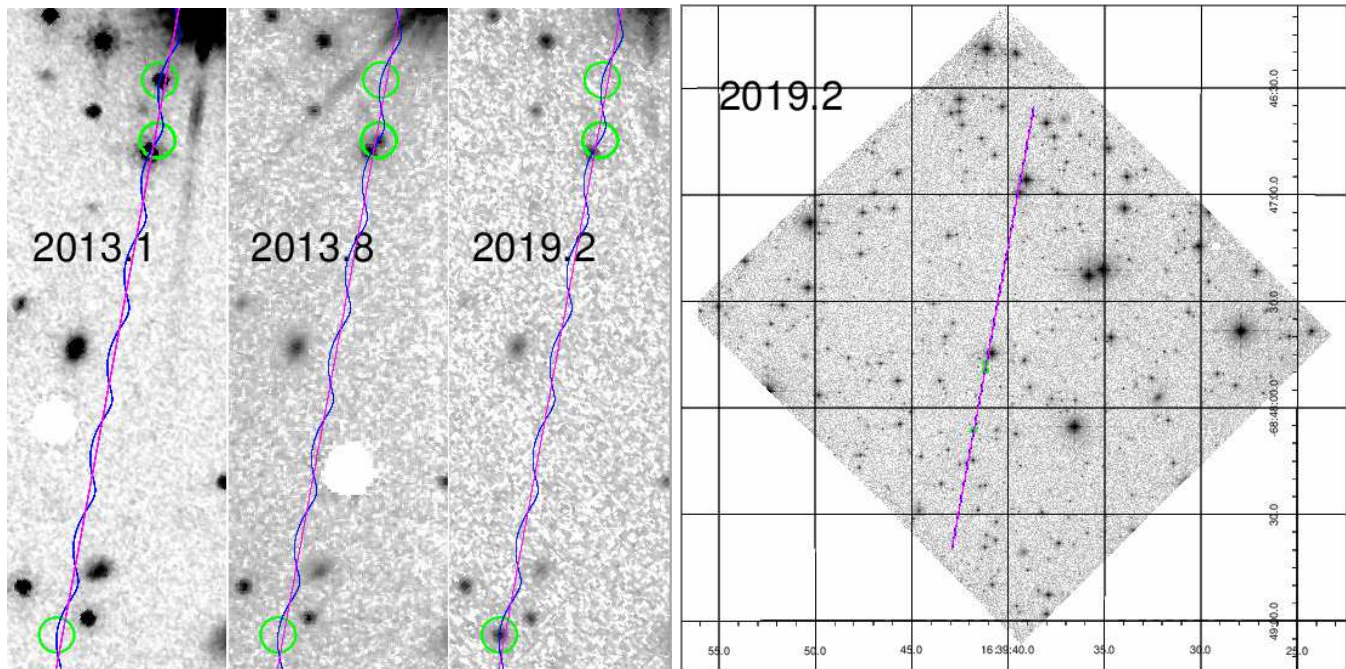


Figure 1. (*Left:*) Zoom-in of the *HST* field surrounding W1639–6847, as collected in the three main epochs analysed in this work. This small region has a size of $\sim 7.5'' \times 22.5''$. Green circles indicate the BD positions at the three epochs. Blue and magenta lines show our astrometric solution of the motions (see Sect. 4.3) for this object (with and without parallax) in years from 1990 to 2030. (*Right:*) The entire field of view is about $2' \times 2'$ and this is the stack of four WFC3/IR/F127M images collected in last epoch, where the dither pattern is best. The grid and labels are in equatorial coordinates.

tober 26th and 27th 2013 each consist of 3 dithered, shallow images of duration 127.935 s in the F105W bandpass (SAMP-SEQ=SPARS25 and NSAMP=7) for total exposures of 383.805 s. The data from October 29th 2013 consist of 4 slightly deeper exposures obtained in the F125W filter adding up to a combined exposure time of 986.749 s: 2 images of 277.938 s each using SAMP-SEQ=SPARS25 and NSAMP=13, and 1 exposure of duration 252.937 s with the same SAMP-SEQ sequence and NSAMP=12, and a final image of 177.936 s with NSAMP=9 samples. The rest of these orbits were dedicated to spectroscopic observations, which we do not consider in this work.

The final, most recent epoch consists of one *HST* orbit, split between the F127M and F139M filters, the combination of these two bandpasses being highly suited to identify substellar objects through a deep water absorption feature (see Fontanive et al. 2018 for details). In each filter, 4 dithered images of equal duration (327.939 s) were acquired in MultiAccum mode, with SAMP-SEQ=SPARS25 and NSAMP=15, for a total exposure time of 1311.756 s in each band. Due to the faintness of our target in the F139M filter, only the F127M data is considered in the astrometric analysis presented in this work.

Therefore, a total of 18 individual images (4+3+3+4+4) are employed for the analysis described in the following.

4 ANALYSIS

We first briefly summarise the data reduction and analyses described in Paper I.

We have extracted positions and magnitudes in every single WFC3/IR FLT image with the software developed by J. Anderson (Anderson & King 2006) and publicly available for WFC3/IR.¹ This software also produces a quality-of-fit parameter (Q ; Anderson et al. 2008) that essentially measures how well the flux distribution resembles the point-spread-functions (PSFs). In these data sets, the parameter Q is close to 0.02 for the best measured stars, degrading to $Q \sim 0.75$ for the faintest stars. Artefacts, resolved galaxies, and compromised or blended measurements always have larger Q values compared to point sources of a same brightness. The derived positions for detected sources are in raw pixel coordinates and are then corrected for the nominal distortion of the camera, which is also publicly available¹.

Given the expected highest signal-to-noise ratio for the sources measured in images from the first epoch, we choose 2013.12427 (Feb. 15th, 2013) as our reference epoch. Four images are available for epoch 2013.12427. The distortion-corrected positions for the sources measured in all four images are combined to compute a more robust estimate of their relative positions. This provides us with 436 sources defining our reference frame (X, Y).

Next, we link our (X, Y) reference frame to Gaia DR2 (Gaia Collaboration et al. 2016, 2018), in order to transform our measured positions into the ICRS. To do that, Gaia DR2 (α, δ) sources positions, which are given at epoch 2015.5, are first re-positioned at the 2013.12427 epoch using (when available) the tabulated proper motions (pms) of those sources. Then a tangent point is adopted, and the co-

¹ <http://www.stsci.edu/~jayander/WFC3/>

ordinates on the tangent plane (ξ, η) are computed. At this point, for all common sources, it becomes possible to compute the most general linear transformations to transform any measured position on the master frame into the tangential plane, and then those positions on the tangential plane via trivial transformations (see equations 1-4 in Paper I) into the ICRS. We initially consider all sources in our master frame, including those with no pms in the Gaia DR2 catalog. Once the match is found, we then restrict this sample to sources that are not saturated in the first epoch images, have Gaia DR2 pms, and have positions consistent within at most 0.03 WFC3-pixels (i.e., 3.6 mas, for the pixel scale 120.9918 mas derived from this transformation, see Section 3.4 of Paper I) between Gaia DR2 at the reference epoch and the reference system. This reduced our available number of common sources to 55.

Finally, measured positions in all the images from all epochs can be linked to the very same reference frame (X, Y), now made of Gaia DR2 sources that can be re-positioned to the corresponding epoch using the tabulated pms. This enables us to transform to the ICRS the positions of every measured object (including sources much fainter than those detectable in Gaia), in every single image, of every single epoch. We refer the reader to Paper I for a more extensive description of the entire procedure.

4.1 Improving the method

In our previous work, when re-positioning the Gaia DR2 sources at the corresponding epoch of each individual image, we only considered the pms –and not the parallaxes. However, the reference sources are all at a finite and different distance, which if ignored would inevitably lead to underestimates in the absolute parallax of the target. Given the size of the uncertainty (~ 2 mas) in the parallax of the target of Paper I (WISE J154151.65–225024), and the already complicated nature of the method, we opted to not add in that work the further complication of dealing with the individual parallaxes of the reference sources. Instead, we simply applied an *a posteriori* correction from relative-to-absolute for the target parallax, which was of the order of 0.2 mas (i.e., $\ll 2$ mas), and taken as the median of the Gaia DR2 parallaxes of the reference objects (after rejecting the one with the most significant parallax).

Now that the bulk of the procedure has been presented in Paper I, we further refine our method and develop the procedure to include the parallaxes of all the reference sources as well. As we will see, this will turn out to be a rather unnecessary step given the currently available data for the specific case of W1639–6847 analysed in the present paper. Nevertheless, it is the appropriate occasion to improve the method in order to obtain absolute astrometric parameters, which might be a necessity for future applications with data sets of higher precisions.

First of all, we need to consider only the sources in Gaia DR2 that, in addition to positions and proper motions, have also a parallax estimate, and then compute their astrometric place at each of the observation epochs, this time including their parallaxes. To compute the positions of the sources in the reference frame, we make use of the sophisticated tool developed by U.S. Naval Observatory, the

Naval Observatory Vector Astrometry Software, hereafter **NOVAS** (in version F3.1, Kaplan et al. 2011), which accounts for many subtle effects, such as the accurate Earth orbit, perturbations of major bodies, nutation of the Moon-Earth system, etc.

In particular, we employ the **NOVAS**'s subroutine **ASSTAR**, which computes the astrometric place of a star. This subroutine takes as input for a source: the ICRS coordinates at epoch 2000.0, the proper motions, the parallax and the radial velocity (RV, which we set identically to $RV=0.0 \text{ km s}^{-1}$ for all sources). The routine in turn produces –at a specified location in the Solar System– the astrometric place of the source in right ascension and declination, at a specified Julian date. Therefore, as Gaia DR2 ICRS positions are given at the epoch 2015.5, we first need to re-position ICRS coordinates to epoch 2000.0, by using Gaia DR2 pms, before passing them to the **ASSTAR** subroutine.

The need for an existing parallax measurement (and with a positive value) significantly restricts the sample of usable Gaia DR2 sources. Most of the images have over 20 Gaia DR2 sources detected on them satisfying these criteria, with a maximum of 25 and a minimum of 14 common sources. Nevertheless, even the image with the minimum number of detected sources in common with Gaia DR2, i.e., 14, has $14 \times 2\text{D}$ positions that are more than adequate to constrain the six parameters of the most general linear transformation to bring those detected positions on that individual image into the ICRS, at the sub-mas level. [Note that for a six parameter transformation, $3 \times 2\text{D}$ data points would be sufficient.] We are thus able to exploit the Gaia DR2 reference sources in each of the 18 individual images employed in this work to carefully study the motion in the field surrounding W1639–6847.

4.2 Stack Images

With the coordinate transformations from each image to the reference frame (X, Y) we can create stacked images within each epoch, and for each filter. Stacked images give the best view of the astronomical scene that can be used to independently check the nature of sources in images. On left panel of Fig.1, we show the obtained stacks for the three main epochs for the two filters with a similar effective wavelength, i.e., F125W (for 2013.1 and 2013.8) and F127M (for 2019.2), in the patch of sky crossed by W1639–6847 between these epochs. The right panel shows the entire field of view for the F127M observations.

We saved our stacked images in **fits** format, and put in their headers our absolute astrometric solution with keywords for World Coordinate System. These five stacked images –one for each filter/epoch combination– are released as supplementary electronic material of this work. Note that the (X, Y) coordinates in this paper are not in the same pixel-coordinate system of these stacked images, which are instead super-sampled by a factor two (i.e., each pixel is ~ 60 mas in size).

4.3 Determination of the Astrometric Parameters

Our 18 images (in 2D) gave 36 individual data points, from which to extract the five astrometric parameters: positions (X, Y) , proper motions (μ_X, μ_Y) and parallax (ϖ) for W1639–6847. As motivated in Paper I, we keep our calculations in the observational plane (X, Y) .

Again, **NOVAS** is used to predict the astrometric place of W1639–6847. We then use a Levenberg-Marquardt algorithm (the FORTRAN version **lmdif** available under **MINIPACK**, Moré et al. 1980) to find the minimisation of the [observed–calculated] values for the five parameters: X, Y, μ_X, μ_Y , and ϖ .

Our best-fit astrometric solution is given in Table 1 and shown in Fig. 2. We note that the estimated parallax is already in an absolute reference system. To assess the uncertainties of our solution we perform 25 000 simulations, adding random errors following Gaussian distributions with dispersion derived from the observed data of W1639–6847 for each of the five filter/epoch combinations (i.e., F125W@2013.1, F105W@2013.812, F105W@2013.820, F125W@2013.826, and F127M@2019.2). The intrinsic ~ 0.050 mas systematic uncertainties inherent to the Gaia DR2 parallaxes (Lindgren et al. 2018) need to be added to the error budget, although completely insignificant compared to the estimated errors on the parallax.

We note that the two epochs with the widest time-baseline also have the best astrometric accuracies and are taken almost exactly at the same phase of the year, making our pms exquisitely accurate, at a quart-of-a-mas level. However, with only three phases of the year mapped, the parallax estimate relies entirely on (and is therefore limited by) the weakest measurements at epochs ~ 2013.8 .

The astrometric precisions at this epoch are, unfortunately, significantly worse than those at the other two epochs for several reasons. First, all images within this epoch are affected by contaminating light coming primarily from scattered Earthlight. This anomaly is often present for IR observations made when the limb angle, which is the angle between *HST*’s pointing direction and the nearest limb of the bright Earth, is less than ~ 30 degrees. Second, the total exposure times, and therefore the average signal to noise ratios in each of these images are significantly lower than for those taken in 2013.1 and 2019.2. Third, the close proximity of a relatively bright star at ~ 3.5 pixels from W1639–6847 might also have contributed to enlarge the errors (see Fig. 1).

In addition to Fig. 2 and its insets, we show in Fig. 3 the parallax ellipse along with *HST* measurements [proper motion subtracted]. This representation better reveals the sampling of the parallactic motion which, with only three main epochs, could be problematic. The fact that the 2013.8 epoch is made of three sub-epochs separated by about a day (on 26, 27 and 29 October 2013, respectively) slightly alleviates this problematic situation in the parallax estimate. While our parallax best fit provides a *formal* error of only ~ 2 mas, a close look at our best-fit compared to the observed points at these ~ 2013.8 epochs seems to suggest a marginally larger parallax, which could be larger by as much as ~ 0.04 WFC3/IR pixel (i.e., ~ 5 mas), or possibly residuals caused by the closeness to the aforementioned field-star at ~ 3.5 pixels in that epoch. Indeed, with only 3 main annual

Table 1. Astrometric parameters of W1639–6847 in the ICRS. Positions are given at 2000.0 and at the Gaia DR2 2015.5 epoch, where the ϖ suffix indicates that the apparent positions have the annual parallax included.

$\alpha_{2000.0}$ [h m s]	16:39:39.72931	± 11 mas
$\delta_{2000.0}$ [° ′ ″]	−68:47:06.69404	± 5 mas
$\alpha_{2000.0}$ [degrees]	249.9155388	± 11 mas
$\delta_{2000.0}$ [degrees]	−68.78519279	± 5 mas
$\alpha_{2015.5}$ [degrees]	249.9224084	± 4.5 mas
$\delta_{2015.5}$ [degrees]	−68.79857156	± 0.8 mas
$\alpha_{\varpi_{2015.5}}$ [degrees]	249.9223335	± 6.6 mas
$\delta_{\varpi_{2015.5}}$ [degrees]	−68.79860735	± 1.5 mas
$\mu_{\alpha \cos \delta}$ [mas yr ^{−1}]	+577.21	± 0.24
μ_{δ} [mas yr ^{−1}]	−3108.39	± 0.27
ϖ [mas]	210.35	$\pm 1.82 \pm 0.05$

phases probed, it is hard to highlight the presence of unaccounted systematic errors in these values. A single future measurement could be sufficient to significantly refine and consolidate our new parallax estimate.

4.4 Improved- vs. old-method, and RVs

Even if we expect negligible differences for the case of W1639–6847, it is worth comparing the numerical results of our procedure from Paper I with the new procedure presented in this work, which includes the parallaxes for the Gaia DR2 reference sources.

In our first test, we performed the astrometric parameters fit using the very same sample of reference stars in each image (14–25), but this time not including their parallaxes (i.e., assuming them to be at infinite distances, therefore setting their parallaxes to zero). We obtained a parallax of $\pi=209.74$ mas, which is slightly smaller than the value $\varpi=210.35$ mas obtained in Table 1. This reduced parallax for W1639–6847 goes in the right direction, meaning that it is an apparent parallax (π) which is obtained with respect to reference sources that are not at infinite distances. Therefore, π is smaller than the absolute parallax (ϖ), as it does not contain the parallax of the references sources, hence expected to be smaller. However, it is only a marginally smaller value, as ~ 0.6 mas compared with an estimated uncertainty for ϖ of 1.8 mas (1- σ) corresponds to a $\sim 0.3\sigma$ significance. Finally, we note that all the other astrometric parameters (positions, and proper motions) show even less significant changes.

As a second test, we compute transformations using all the Gaia DR2 stars with proper motions, even when no (positive) parallaxes were available. This results in an enlarged sample of reference objects (57-79 vs. 14-25). The derived apparent parallax in this case is $\pi=210.02$ mas, thus even closer (~ 0.3 mas) to our derived absolute parallax ($\varpi=210.35$ mas), and consistent with it at the $\sim 0.2\sigma$ -level. We note that the consistency in positions between Gaia DR2 stars and their positions in the *HST* images are always bet-

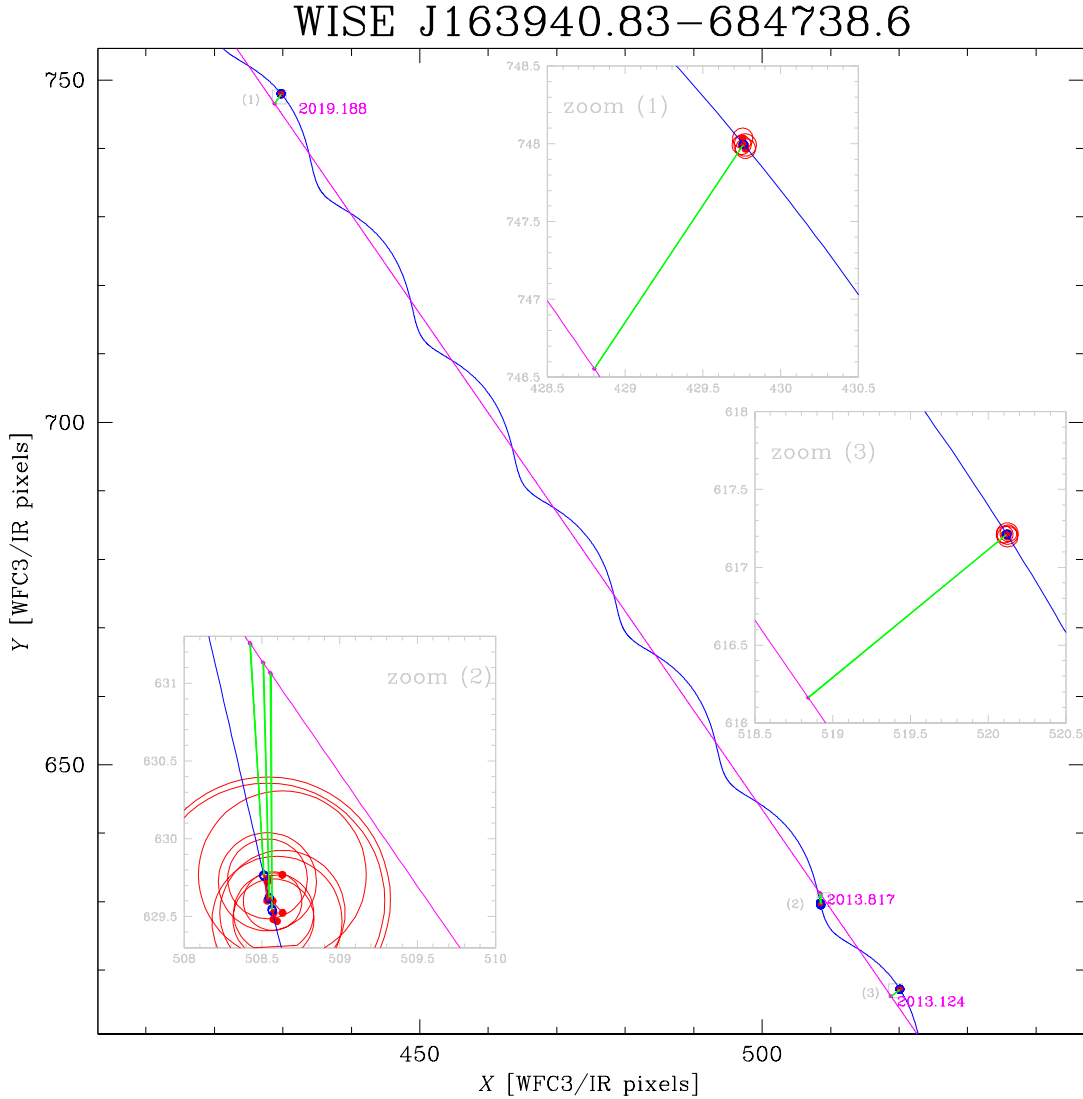


Figure 2. Comparison of our astrometric solution (line in blue) with the individual observed data points (red bullet) for W1639–6847 in the observational plane $(X, Y)_{2013.12}$. The three major epochs are indicated by labels, and three insets indicated by the gray boxes, with (1), (2) and (3), show a more meaningful zoom-in of the data points. Red circles indicate the quality fit (Q) for each data point, with smaller values for better measurements. To better highlight the parallax component of the motion, a line in magenta indicates an object with the same motion but at infinite distance. Green lines show the parallax contributions at each epoch, and red segments connect the individual data points with their expected positions (on the blue line) according to the best fit.

Table 2. List of works in the Literature providing astrometric parameters for W1639–6847.

work #. authors (date)	$\mu_{\alpha^*} \pm \sigma_{\mu_{\alpha^*}}$ [mas yr ⁻¹]	$\mu_{\delta} \pm \sigma_{\mu_{\delta}}$ [mas yr ⁻¹]	$\varpi \pm \sigma_{\varpi}$ [mas]	d [pc]	source facilities
1. Tinney et al. (2012)	580 ± 22	-3013 ± 40	200 ± 20	5.0 ± 0.5	Magellan+ <i>WISE</i>
2. Tinney et al. (2014)	586.0 ± 5.5	-3101.1 ± 3.6	202.3 ± 3.1	4.9 ± 0.1	Magellan
3. Pinfield et al. (2014)	-800 ± 1200	-2800 ± 1200	<i>WISE</i>
4. Martin et al. (2018)	579.09 ± 12.52	-3104.54 ± 12.25	228.05 ± 8.93	$4.39^{+0.18}_{-0.17}$	<i>Spitzer</i>
5. Kirkpatrick et al. (2019)	582.0 ± 1.5	-3099.8 ± 1.5	211.9 ± 2.7	4.72 ± 0.06	<i>Spitzer</i>
6. this work	577.21 ± 0.24	-3108.39 ± 0.27	210.35 ± 1.82	4.75 ± 0.05	<i>HST+Gaia</i>

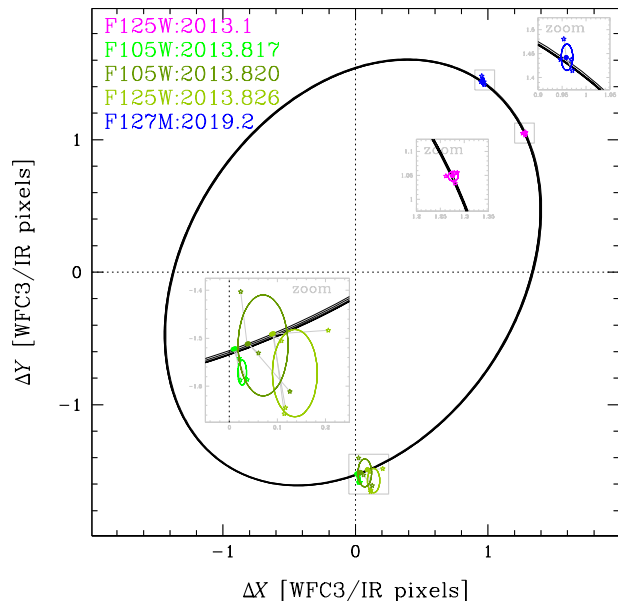


Figure 3. Our solution for the parallax ellipse in the $(X, Y)_{2013.12}$ coordinate system. Individual *HST* data points are indicated with star symbols, which are connected with small segments to their expected positions according to our best fit. Smaller ellipses in magenta, green, and blue, indicate the $1\text{-}\sigma_{X,Y}$ of individual data points within each epoch. Note how ellipses are significantly smaller for the first and last epochs, compared to the 2013.8 sub-epochs. Insets in gray have the same scale, and show zoom-in views around the locations marked by gray boxes.

ter than ~ 3 mas (Paper I, Fig. 3, as well as this work), and that the inconsistencies are dominated by random errors in the positions measured in the *HST* images. Therefore, going from ~ 20 to ~ 70 reference sources we could hope to reduce the errors in our transformations (from the image coordinates system of the *HST* individual images to the Gaia DR2 system) at most from ~ 0.65 mas to ~ 0.35 mas, which are both well within the uncertainties of our individual measurements, and also within the errors in our fitted absolute parallax, $\sigma_{\varpi} = 1.8$ mas.

In our third and last test, we explore the impact of RVs on our final astrometry. In our derivations of the astrometric parameters, we have assumed the RVs for all the stars, W1639–6847 included, to be identically zero. However, a non-null radial velocity means that objects change in time their distance with respect to the observer, and therefore change their parallax in time, as result of projection effects. Essentially all reference stars in our studied field are significantly further away than our science target. Therefore neglecting their RVs has a much smaller effects than neglecting the target RV, as their distances will change by much less in percentage than for W1639–6847. Assuming arbitrary RV values for the target simply cause fluctuations of our fit within the noise, for RVs up to ± 1000 km s $^{-1}$. This is not surprising, as even for the most extreme case of the *Barnard’s Runaway Star*, which has an RV of -110.6 km s $^{-1}$ and a $\varpi = 547.45$ mas, we expect a parallax change rate of only $\dot{\varpi} = +34$ μ as yr $^{-1}$ (Dravins et al. 1999).

Nevertheless, it is interesting to note that astrometry could be used, *in turn*, to estimate RVs, and that these astrometric-RVs do not suffer from spectroscopic biases such as gravitational redshifts (as high as 25 km s $^{-1}$ for WDs), convective bubble motions (~ 0.5 km s $^{-1}$ for red giants), etc. (indeed, any spectroscopic measurement is always model-dependent, while astrometry is a purely geometrical one). The secular changes of trigonometric parallaxes are well known effects that can be used to determine model-independent astrometric-RVs (see paper series by Dravins et al. 1999 for a review). Astrometric-RVs are well within the reach of *Gaia* precision for several close-by (or fast-moving) stars, but extremely hard to measure with traditional *HST* images (at least in non-trailing mode).

5 CONCLUSIONS

In this work, we have perfected the procedure developed in Paper I (Bedin & Fontanive 2018) exploiting the power of Gaia DR2 to improve imaging-astrometry with narrow-field cameras. Our method makes use of the positions, proper motions and parallaxes of stars in the Gaia DR2 catalog to derive highly-precise astrometric solutions for sources too faint for Gaia observed in multiple epochs of *HST* data. The technique was refined in this paper to include the Gaia DR2 parallaxes of the astrometric reference sources in the analysis, allowing us to directly obtain absolute astrometric parameters.

This improved procedure was applied to the brown dwarf WISE J163940.83–684738.6, a Y0pec dwarf with puzzling photometric and spectroscopic features. The distance and proper motion of this unusual object are poorly constrained, with significant inconsistencies between existing estimates. Using three epochs of *HST*/WFC3 data acquired over a period of ~ 6 years, we were able to constrain its parallax to $\varpi = 210.4 \pm 1.8$ mas, and its proper motion to $\mu_{\alpha \cos \delta} = 577.21 \pm 0.24$ mas yr $^{-1}$, $\mu_{\delta} = -3108.39 \pm 0.27$ mas yr $^{-1}$.

With achieved precisions of ~ 2 mas in parallax and at the sub-mas level in proper motion, these new astrometric parameters represent considerable improvements relative to previous estimates, as summarised in Table 2. On one hand, our proper motion measurements are in good agreement with other estimates from the literature. In particular, our derived $\mu_{\alpha \cos \delta}$ and μ_{δ} values are consistent with the results from Tinney et al. (2014) and Martin et al. (2018) within 2σ , although our obtained uncertainties are smaller by more than an order of magnitude. On the other hand, larger disparities ($>3\sigma$) are observed between our proper motion measurements and those from Kirkpatrick et al. (2019), which were the most accurate to date.

Our estimates of the astrometric parameters for W1639–6847 are completely independent from the ones obtained with *Spitzer* data, and because of this, have an important value on their own. For the same reason it would also be interesting to combine them properly. Indeed, while unaccounted systematic errors in our estimated parallax could be as large as ~ 5 mas, due to the problematic epochs around 2013.8 (see Sect 4.3), based on our experience we can hardly expect residual systematic errors larger than 1 mas yr $^{-1}$ in the estimated proper motions derived

from *HST* data (e.g., Bellini et al. 2018 and reference therein). As we do not have the competence to analyse *Spitzer* data at the same level of accuracy as we have done for the *HST* data (not only distortion and positioning, but particularly the way to simultaneously fit *HST* data with data from a telescope in a significantly different, Earth-trailing, Heliocentric orbit), we list in Table 3 our *HST* individual measurements to allow future investigators to be able to properly combine the two space-based datasets.

In terms of parallax, results from previous works were more discordant, with a $\sim 10\%$ discrepancy between the best available estimates so far (Tinney et al. 2014; Martin et al. 2018; Kirkpatrick et al. 2019). Interestingly, our newly-derived value was found to be somewhere in between the ground-based and *Spitzer* determinations from Tinney et al. (2014) and Martin et al. (2018), respectively, and this time in excellent agreement with the *Spitzer*-derived value from Kirkpatrick et al. (2019), which used additional epochs of data compared to the work from Martin et al. (2018). The corresponding distance of 4.75 ± 0.05 pc we obtained here for W1639–6847 makes our result the most accurate distance measurement available for this Y dwarf.

As previously discussed, our parallax estimate for W1639–6847 relies entirely on the epoch with the lowest astrometric precision, and will require an additional epoch of observations to be further validated and refined. An accurate measurement of the distance to W1639–6847 will certainly be the key to modelling and understanding the peculiar atmospheric characteristics observed to date for this object. Nevertheless, we have successfully demonstrated that our powerful procedure allows us to place strong constraints on the parallax and proper motion of extremely faint objects, based on only three epochs of observations taken over a baseline of \sim half a decade.

The *Hubble Space Telescope* indeed provides a unique opportunity to reach such results for faint and red brown dwarfs, with an ideal compromise between the ~ 121 mas plate scale of the WFC3/IR channel and the wide field of view allowing for numerous astrometric references, combined with the exquisite stability achieved from space. In contrast, other space-based telescopes generally have significantly broader pixel sizes ($>1-2$ arcsec), leading to lower astrometric resolutions and increased chances of blended sources (like it was originally the case for our target W1639–6847 in *WISE*; Tinney et al. 2012). While ground-based facilities typically have much higher angular resolutions, mitigating the broad plate scale drawbacks, observations from the ground are constrained by sensitivity, rendering observations of the faintest brown dwarfs extremely challenging. In addition, ground-based data generally suffer from atmospheric aberrations and numerous systematic errors that can be difficult to quantify and account for when comparing between near-infrared brown dwarf targets and field stars of very different colours.

HST therefore represents a superior platform for high-precision astrometry of ultracool dwarfs, and for a method like the one developed in this paper to be applied. The derivation of new distance measurements for a number of additional Y brown dwarfs via such an approach will be crucial to the characterisation of these objects, and will undoubtedly

shed new light on substellar studies, at the individual and population levels.

The remarkable spatial and spectral resolution of the anticipated *James Webb Space Telescope (JWST)* will soon allow for unparalleled probes of ultracool brown dwarfs at near-infrared wavelengths, by observing at wavelengths where Y dwarfs are orders of magnitude brighter than they are at *HST* wavelengths. In particular, between the very large field of view of the Near Infrared Camera (NIRCam) instrument and its exceptional angular resolution of 32 mas at $2 \mu\text{m}$, we will be able to take our technique a step further with *JWST*, and measure precise distances to the coldest objects in the Solar neighbourhood to even greater accuracies. This will in turn tremendously enhance our understanding of planet-like atmospheres and will provide unique opportunities to calibrate theoretical models at the low-mass end of the substellar regime.

ACKNOWLEDGEMENTS

We thank an anonymous Referee for the useful comments, the tests suggested, and for the prompt review of our work. This work is based on observations with the NASA/ESA Hubble Space Telescope, obtained at the Space Telescope Science Institute, which is operated by AURA, Inc., under NASA contract NAS 5-26555. This work makes also use of results from the European Space Agency (ESA) space mission Gaia. Gaia data are being processed by the Gaia Data Processing and Analysis Consortium (DPAC). Funding for the DPAC is provided by national institutions, in particular the institutions participating in the Gaia MultiLateral Agreement (MLA). The Gaia mission website is <https://www.cosmos.esa.int/gaia>. The Gaia archive website is <https://archives.esac.esa.int/gaia>. This research has benefitted from the Y Dwarf Compendium maintained by Michael Cushing at <https://sites.google.com/view/ydwarfcompendium/>. LRB acknowledges support by MIUR under PRIN program #2017Z2HSMF.

REFERENCES

- Allen P. R., Koerner D. W., Reid I. N., Trilling D. E., 2005, *ApJ*, 625, 385
- Anderson J., King I. R., 2006, Technical report, PSFs, Photometry, and Astronomy for the ACS/WFC
- Anderson J., et al., 2008, *AJ*, 135, 2055
- Bedin L. R., Fontanive C., 2018, *MNRAS*, 481, 5339
- Beichman C., Gelino C. R., Kirkpatrick J. D., Cushing M. C., Dodson-Robinson S., Marley M. S., Morley C. V., Wright E. L., 2014, *ApJ*, 783, 68
- Bellini A., et al., 2018, *ApJ*, 853, 86
- Burgasser A. J., 2004, *ApJS*, 155, 191
- Chiu K., Fan X., Leggett S. K., Golimowski D. A., Zheng W., Geballe T. R., Schneider D. P., Brinkmann J., 2006, *AJ*, 131, 2722
- Cruz K. L., et al., 2007, *AJ*, 133, 439
- Cruz K. L., Kirkpatrick J. D., Burgasser A. J., 2009, *AJ*, 137, 3345

- Cushing M. C., et al., 2011, *ApJ*, 743, 50
Dravins D., Lindegren L., Madsen S., 1999, *A&A*, 348, 1040
Dupuy T. J., Kraus A. L., 2013, *Science*, 341, 1492
Dupuy T. J., Liu M. C., 2012, *ApJS*, 201, 19
Faherty J. K., et al., 2012, *ApJ*, 752, 56
Fontanive C., Biller B., Bonavita M., Allers K., 2018, *MNRAS*, 479, 2702
Gaia Collaboration et al., 2016, *A&A*, 595, A1
Gaia Collaboration et al., 2018, *A&A*, 616, A1
Kaplan G., Bartlett J., Monet A., Bangert J., Puatua W., 2011. User's Guide to NOVAS Version F3.1. USNO, Washington, DC
Kirkpatrick J. D., et al., 2011, *ApJ*, 197, 19
Kirkpatrick J. D., et al., 2012, *ApJ*, 753, 156
Kirkpatrick J. D., et al., 2019, *ApJS*, 240, 19
Knapp G. R., et al., 2004, *AJ*, 127, 3553
Leggett S. K., Tremblin P., Esplin T. L., Luhman K. L., Morley C. V., 2017, *ApJ*, 842, 118
Lindegren L., et al., 2018, *A&A*, 616, A2
Liu M. C., et al., 2011, *ApJ*, 740, 108
Liu M. C., Dupuy T. J., Allers K. N., 2016, *ApJ*, 833, 96
Manjavacas E., Goldman B., Reffert S., Henning T., 2013, *A&A*, 560, A52
Manjavacas E., et al., 2019, *AJ*, 157, 101
Martin E. C., et al., 2018, *ApJ*, 867, 109
Moré J. J., Garbow B. S., Hillstrom K. E., 1980. User Guide for MINPACK-1. Argonne National Laboratory Report ANL-80-74, Argonne, IL
Opitz D., Tinney C. G., Faherty J. K., Sweet S., Gelino C. R., Kirkpatrick J. D., 2016, *ApJ*, 819, 17
Pinfield D. J., Jones H. R. A., Lucas P. W., Kendall T. R., Folkes S. L., Day-Jones A. C., Chappelle R. J., Steele I. A., 2006, *MNRAS*, 368, 1281
Pinfield D. J., et al., 2014, *MNRAS*, 437, 1009
Schneider A. C., et al., 2015, *ApJ*, 804, 92
Schneider A. C., Cushing M. C., Kirkpatrick J. D., Gelino C. R., 2016, *ApJ*, 823, L35
Tinney C. G., Faherty J. K., Kirkpatrick J. D., Wright E. L., Gelino C. R., Cushing M. C., Griffith R. L., Salter G., 2012, *ApJ*, 759, 60
Tinney C. G., Faherty J. K., Kirkpatrick J. D., Cushing M., Morley C. V., Wright E. L., 2014, *ApJ*, 796, 39
Zalesky J. A., Line M. R., Schneider A. C., Patience J., 2019, *ApJ*, 877, 24

Table 3. (*only for the on-line version*): For each of the 18 *HST* images analysed in this work we list: the Modified Julian day, our estimated coordinates for W1639–6847 in the ICRS at the epoch of the image, its positions on the master frame (X, Y), the image archival root-name, and finally the measured raw coordinates of the target in pixel for that image.

ID	MJD	α	δ	X	Y	image-rootname	x_{raw}	y_{raw}
01	56338.14155198	249.92151060	−68.79651910	520.1296	617.2179	ic2j11yyq	449.559	615.940
02	56338.14924864	249.92151018	−68.79651922	520.1237	617.2174	ic2j11yzq	453.569	617.449
03	56338.15694568	249.92150860	−68.79651953	520.1053	617.2117	ic2j11z1q	452.086	619.960
04	56338.16464235	249.92150890	−68.79651873	520.1244	617.1972	ic2j11z3q	448.114	618.487
05	56591.14584568	249.92156200	−68.79708433	508.5961	629.4704	ic2j45z9q	477.380	467.188
06	56591.27527865	249.92156403	−68.79708609	508.5746	629.5227	ic2j45zdq	481.273	468.689
07	56591.35626235	249.92156125	−68.79708516	508.5731	629.4820	ic2j45zhq	479.694	471.232
08	56594.40066068	249.92157595	−68.79709224	508.5353	629.7427	ic2j47ksq	476.855	466.750
09	56594.46119883	249.92158388	−68.79709057	508.6305	629.7683	ic2j47kwq	480.756	468.302
10	56594.52770920	249.92156746	−68.79708904	508.5383	629.6109	ic2j47l1q	479.373	468.307
11	56594.59408642	249.92156657	−68.79708896	508.5332	629.6024	ic2j47l6q	475.339	469.327
12	56592.33998921	249.92157465	−68.79709182	508.5343	629.7240	ic2j97dkq	476.875	466.871
13	56592.40320679	249.92156871	−68.79708806	508.5685	629.5998	ic2j97doq	480.947	468.535
14	56592.46956087	249.92156782	−68.79708475	508.6315	629.5236	ic2j97dsq	479.455	471.111
15	58553.04026694	249.92420535	−68.80177153	429.7715	747.9917	id1223a9q	437.922	746.113
16	58553.04482694	249.92420714	−68.80177292	429.7556	748.0347	id1223adq	458.795	753.869
17	58553.04938731	249.92420398	−68.80177094	429.7734	747.9690	id1223afq	446.587	774.120
18	58553.05394731	249.92420389	−68.80177209	429.7485	747.9923	id1223ahq	425.689	766.439